Lagrangian Coherent Structures in three-dimensional flows

João H Bettencourt, Cristóbal López and Emilio Hernández-García

IFISC (CSIC-UIB), Instituto de Física Interdisciplinar y Sistemas Complejos
Campus Universitat de les Illes Balears
E-07122 Palma de Mallorca, Spain

E-mail: `joaob@ifisc.uib-csic.es`

Abstract.
Lagrangian Coherent Structures (LCS) act as the organizers of transport in fluid flows and are crucial to understand their stirring and mixing properties. In the case of oceanic flows, LCS are known to drive biological dynamics, from plankton to top predators, which stresses the importance of their characterization in realistic flows. Lyapunov exponents are useful tools to compute LCSs. In this paper we have used the Finite-Size Lyapunov Exponent (FSLE) to identify LCSs in two different types of three-dimensional turbulent velocity fields. First, in a canonical turbulent flow (channel flow between two parallel plates) the LCSs have a complex three-dimensional shape and are advected by the flow. Second, in an oceanographic setting (a regional simulation of the Benguela area) the LCSs also show a complex pattern on the horizontal but the small vertical velocities typical of oceanic flows result in a *curtain*-like shape.

arXiv:1207.1975v1 [nlin.CD] 9 Jul 2012

1. Introduction

The use of stretching quantifiers such as the Lyapunov exponents, which measure the relative separation of transported particles [1, 2, 3, 4], has largely improved the Lagrangian analysis of fluid flows. On the one hand Lyapunov methods provide information on time scales for dispersion processes, with its relevance for mixing and stirring of fluids [1, 2, 3, 5, 6, 7]. On the other, they are useful to detect the so-called Lagrangian Coherent Structures (LCS). LCSs [8, 9] are templates for particle advection in complex flows, separating regions with different dynamical behavior and signalling the existence of barriers and avenues to transport, fronts or eddy boundaries [9, 3, 4, 10, 6, 11, 12, 13].

The relationship of LCSs with ridges (local maxima) of Lyapunov fields has been soundly established for the case of finite-time Lyapunov exponents (FTLEs) [14, 15], although it should be mentioned that techniques more precise than Lyapunov methods are available [11, 16]. In our work, we use instead finite-size Lyapunov exponents (FSLEs), which quantify the separation rate of fluid particles between two given distance thresholds [1, 2]. They turn out to be convenient for the case of bounded flows in which characteristic spatial scales are more direct to identify than temporal ones. Following many previous works [10, 6, 17, 12, 18] we assume that the mathematical results existing for FTLEs are valid for FSLEs to a good approximation. In particular we assume that LCSs can be computed as ridges of FSLEs, and that they are transported by the flow as material surfaces/lines, with no flux of particles through them. Observations presented here are consistent with those assumptions.

Despite its relevance in real flows, the full three-dimensional (3d) structure of LCSs is still an open subject. In 3d flows, LCS were explored in atmospheric contexts [19, 20, 21], and in a turbulent channel flow at $Re_\tau = 180$ in [22]. A kinematic ABC flow was studied in [23]. In the ocean, where it is widely recognized that filamental structures, eddies, and in general oceanic meso- and submeso-scale structures have a great influence on marine ecosystems [24, 25, 26, 27], the identification of LCSs and the study of their role in the transport of biogeochemical tracers has primarily been restricted to the two-dimensional (2d) surface layers. There are two concurrent reasons for this: a) because of stratification and rotation, vertical motions in the ocean are usually very small when compared to horizontal displacements; b) synoptic measurements (e.g. from satellites) of relevant quantities are restricted to the surface. A few previous results for Lagrangian eddies in 3d were obtained in Refs. [28, 29], by applying the methodology of lobe dynamics and the turnstile mechanism. Also, Refs. [30, 31] used 3d FSLE fields to identify LCS in oceanic flows. In particular, a mesoscale eddy in the Southern Atlantic was studied in [31], and it was shown that oceanic LCSs presented a vertical curtain-like shape, i.e. they look mostly like vertical sheets, and that material transport into and out of the mesoscale eddy occurred through filamentary deformation of such structures.

In this paper, we use 3d fields of FSLE to identify LCSs in a turbulent channel flow and in an oceanic flow. Observations of the similarities and differences between the two

systems, both in their computation and their physical meaning, helps to appreciate the power and scope of this Lagrangian technique in the analysis of fluid flows. In Section 2 we describe the methodology used to identify LCSs in 3d turbulent flows. Sections 3 and 4 are devoted to the turbulent channel flow and the oceanic flow, respectively, and Section 5 presents conclusions and ideas for future work.

2. Methods

2.1. Finite-Size Lyapunov Exponents

In order to study non-asymptotic dispersion processes such as stretching at finite scales and bounded domains, the finite size Lyapunov Exponent was introduced [1, 2, 3]. It is defined as:

$$\lambda = \frac{1}{\tau} \log \frac{d_f}{d_0}, \tag{1}$$

where τ is the time it takes for the separation between two particles, initially d_0, to reach a value d_f. In addition to the dependence on the values of d_0 and d_f, the FSLE depends also on the initial position of the particles and on the time of deployment. Locations (i.e. initial positions) leading to high values of this Lyapunov field identify regions of strong separation between particles, i.e., regions that will exhibit strong stretching during evolution, that can be identified with the LCS [3, 10, 6].

In principle, to compute FSLE in 3d, the method of [6] can be extended to include the third dimension, by computing the time it takes for particles initially separated by $d_0 = [(\Delta x_0)^2 + (\Delta y_0)^2 + (\Delta z_0)^2]^{1/2}$ need to reach a final distance of $d_f = [(\Delta x_f)^2 + (\Delta y_f)^2 + (\Delta z_f)^2]^{1/2}$. We will proceed this way for the turbulent channel, but, as indicated in [31], vertical displacements are much smaller than horizontal ones in ocean flows. Therefore, the displacement in the z direction does not contribute significatively to the calculation of d_f in the ocean, which prompt us to implement a quasi-3d computation of FSLEs: we use the full 3d velocity field for particle advection but particles are initialized in 2d horizontal ocean layers and the contribution Δz_f is not considered when computing d_f (see more details in [31]). In any case, since we allow the full 3d trajectories of particles, we take into account the vertical dynamics of the oceanic flows.

Concerning the turbulent channel, where we can implement a fully 3d computation of the FSLE, we proceed as follows. A grid of initial locations $\mathbf{x}_0 = (x_i, y_j, z_k)$ is set up at time t, fixing the spatial resolution of the FSLE field (Fig. 1). Particles are released from each grid point and their three-dimensional trajectories are calculated. The distances of each neighbor particle with respect to the central one (initially d_0) is monitored until one of the separations reaches a value d_f.

In both systems considered, we obtain two different types of FSLE maps by integrating the three-dimensional particle trajectories backward and forward in time:
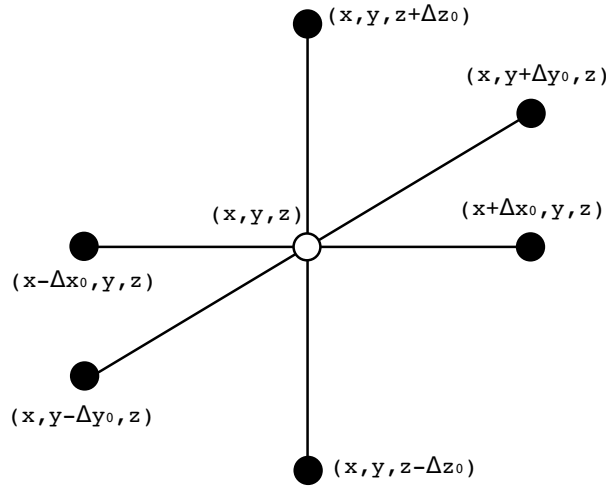
Figure 1. Computational setup for the calculation of the FSLE field in 3d. The FSLE at the location of the central particle ($\circ$) is a measure of the time it takes for any of the neighbor particles ($\bullet$) to diverge from the central particle by a distance greater than δ_f.

the attracting LCSs (for the backward), and the repelling LCSs (forward) [10, 6]. We obtain in this way FSLE fields with a spatial resolution given by d_0. When a particle leaves the velocity field domain or reaches a no-slip boundary, the FSLE value at its initial position and initial time is set to zero. If the interparticle separation remains smaller than δ_f past a maximum integration time Δt, then the FSLE for that location is also set to zero.

2.2. Lagrangian Coherent Structures

The identification of LCS calculated from Lyapunov fields in 2d flows is straightforward since they practically coincide with (finite-time) stable and unstable manifolds of relevant hyperbolic structures in the flow [8, 9, 10] (but see [32, 16]). The structure of these manifolds in 3d is generally much more complex than in 2d [23, 33], and they can be locally either lines or surfaces.

Differently than 2d, where LCS can be visually identified as the maxima of the FSLE field, in 3d they are hidden within the volume data and one needs to explicitly compute and extract them, using the definition of LCSs as the ridges of the FSLE field. A ridge L is a co-dimension 1 orientable, differentiable manifold (which means that for a 3d domain D, ridges are surfaces) satisfying the following conditions [15]:

(i) The field λ attains a local extremum at L.

(ii) The direction perpendicular to the ridge is the direction of fastest descent of λ at L.

This definition means that as we move away from the ridges, perpendicularly to it, we would see the fastest descent of the FSLE field. The method used to extract the ridges from the scalar field $\lambda(\mathbf{x}_0, t)$ is from [34]. It uses an earlier [35] definition of ridge in the

context of image analysis, as a generalized local maxima of scalar fields. For a scalar field $f : \mathbb{R}^n \to \mathbb{R}$ with gradient $\mathbf{g} = \nabla f$ and Hessian $\mathbf{H}$, a d-dimensional height ridge is given by the conditions

$$\forall d < i \leq n \quad , \mathbf{g}^{\mathrm{T}} \mathbf{e}_i = 0 \text{ and } \alpha_i < 0, \tag{2}$$

where $\alpha_i, i \in \{1, 2, \ldots, n\}$, are the eigenvalues of $\mathbf{H}$, ordered such that $\alpha_1 \geq \ldots \geq \alpha_n$, and $\mathbf{e}_i$ is the eigenvector of $\mathbf{H}$ associated with α_i. For $n = 3$, Eq. (2) becomes

$$\mathbf{g}^{\mathrm{T}} \mathbf{e}_3 = 0 \text{ and } \alpha_3 < 0. \tag{3}$$

In other words, in $\mathbb{R}^3$ the $\mathbf{e}_1, \mathbf{e}_2$ eigenvectors point locally along the ridge and the $\mathbf{e}_3$ eigenvector is orthogonal to it, so the the ridge maximizes the scalar field in the normal direction to it and in this direction the field is more convex than in any other direction, since the eigenvector associated with the most negative eigenvalue is oriented along the direction of maximum negative curvature of the scalar field.

The extraction process progresses by calculating the points where the ridge conditions are verified and the ridge strength $|\alpha_3|$ is higher than predefined threshold s so that ridge points whose value of α_3 is lower (in absolute value) than s are discarded from the extraction process. Since the ridges are constructed by triangulations of the set of extracted ridge points, the strength threshold greatly determines the size and shape of the extracted ridge, by filtering out regions of the ridge that have low strength. The reader is referred to [34] for details about the ridge extraction method. The height ridge definition has been used to extract LCS from FTLE fields in several works (see, among others, [36]).

Since the λ value of a point on the ridge and the ridge strength α_3 are only related through the expressions (2) and (3), the relationship between the two quantities is not direct, which makes difficult to choose the appropriate strength threshold s. A too small value of s will result in the extraction of very small LCSs that appear to have little influence on the dynamics, while a large value will result in only a partial rendering of the larger and more significant LCS, limiting the possibility of observing their real impact on the flow.

The ridges extracted from the backward FSLE map approximate the attracting LCSs, and the ridges extracted from the forward FSLE map approximate the repelling LCSs. The attracting ones are the more interesting from a physical point of view [6, 12], since particles (or any passive scalar driven by the flow) typically approach them and spread along them, so that they are good candidates to be identified with the typical filamentary structures observed in tracer advection.

3. Turbulent channel flow

Turbulent channel flow is a flow between two stationary, parallel walls separated by a distance 2δ. It has been studied extensively due to its geometrical simplicity and its wall-bounded nature, which makes it a platform to study more complex turbulent shear flows of greater technological interest.

The coordinates of the flow are: x for the streamwise direction, y for the cross-stream coordinate that separates the two plates, and z for the spanwise direction. The flow is maintained by a downstream pressure gradient $\frac{dP_0}{dx}$ acting against the wall shear stress. The laminar flow solution U_0 is a cross-stream parabolic profile given by

$$U_0(y) = \frac{y^2 - \delta^2}{2\mu} \frac{dP_0}{dx} \ , \tag{4}$$

where μ is the dynamic viscosity. Following the Reynolds averaging method [37], the turbulent flow velocity $\mathbf{u}$ is decomposed in a mean $\mathbf{U} = (U(y), 0, 0)$ and a fluctuating component $\mathbf{u}' = (u', v', w')$. The mean turbulent velocity profile $U(y)$ differs from the laminar one, $U_0(y)$, by a lower centerline velocity $U(0)$ and increased near-wall velocity giving it a flatter shape. Due to the increase in mean velocity near the wall, the shear stress near the wall is higher for the turbulent case. The total shear stress τ appearing in the averaged Reynolds equations gets contributions from both the viscous stress and the Reynolds stress $-\overline{u'v'}$ associated to the velocity fluctuations:

$$\frac{\tau}{\rho} = \nu \frac{dU}{dy} - \overline{u'v'} \tag{5}$$

$\nu = \mu/\rho$ is the kinematic viscosity. The symmetries of the domain and the Reynolds equations imply that τ depends only on the cross-stream coordinate y, and the dependence is linear, so that it can be written as

$$\frac{\tau(y)}{\rho} = u_\tau^2 \left(1 - \frac{y}{\delta} \right) \tag{6}$$

The shear velocity u_τ gives the velocity scale of the turbulent velocity fluctuations. The formula [37]:

$$\rho u_\tau^2 = \mu \left. \frac{dU(y)}{dy} \right|_{y=0} \tag{7}$$

allows to compute u_τ from measurements of the mean velocity profile from the simulations. A length scale can be formed by combining u_τ with ν: the wall scale $\delta^+ = \nu/u_\tau$. The wall distance can now be expressed as $y^+ = y/\delta^+$, and the same normalization could be done for the rest of coordinates. The viscous Reynolds number $Re_\tau = \delta/\delta_+$ is simply the ratio between the two relevant length scales.

The existence of coherent structures in turbulent wall-bounded flows has been known for several decades from investigations on intermittency in the interface between turbulent and potential flow regions, on the large eddy motions in the outer regions of the boundary layer, and on coherent features in the near-wall region ([38] and references therein). Since then, through experimental and numerical investigations, a picture of the organization of these coherent structures in the turbulent boundary layer has emerged, which has become rather complete from the Eulerian point of view [38, 39]. Our approach is a contribution to the Lagrangian exploration of these coherent structures, as in [22].

The longitudinal velocity field in the inner region of the channel (the viscous sublayer adjacent to the wall and the intermediate buffer region) is organized into

alternating streamwise streaks of high and low speed fluid. Turbulence production occurs mainly in the buffer region in association with intermittent and violent outward ejections of low-speed fluid and inrushes of high-speed fluid towards the wall. The outer region is characterized by the existence of three-dimensional δ-scale bulges that form on the turbulent/potential flows interface. Irrotational valleys appear at the edges of the bulges, entraining high-speed fluid into the turbulent inner region. A central element in the structure of the turbulent boundary layer is the hairpin vortex, mainly because it is a structure with the capability of transporting mass and momentum across the mean velocity gradient and because it provides a paradigm with which to explain several observations of wall turbulence [38, 40].

3.1. Data

The data used to extract the LCS come from a direct numerical simulation (DNS) of turbulent channel flow at a viscous Reynolds number $Re_\tau = 180$. The setup of the simulation follows that of [41] and is summarized in table 1. The simulations were conducted using the CFD solver `Channelflow`. The `Channelflow` code solves the incompressible Navier-Stokes equations in a rectangular box with dimensions $L_x \times 2\delta \times L_z$, with periodic boundary conditions in the x (so that fluid leaving the computational domain in the direction of the mean flow at $x = L_x$ reenters it at $x = 0$) and in the spanwise z direction. No-slip conditions are imposed on $y = \pm\delta$. The unsteady velocity field $\mathbf{u}$ is represented as a combination of Fourier modes in the x and z directions and of Chebyshev polynomials in the wall-normal direction. The pressure gradient necessary to balance the friction at the walls was chosen as to maintain a constant bulk velocity of $\frac{2}{3}U_0$. Time stepping is a 3rd-order Semi-implicit Backward Differentiation. Note that in our computations $\delta^+ = 1/Re_\tau = 0.0058$ so that in wall units $0 < y+ < 344$.

The flow was integrated from an initial base-flow with parabolic profile and a small disturbance that evolved into a fully developed turbulent flow. The total integration time was $\Delta t = 600$ time units that in dimensionless form $t^+ = t(u_\tau^2/\nu)$ gives $\Delta t^+ = 83.54$. After an initial transient of about 200 time units the simulations reached a statistically stationary state from which statistics was accumulated.

The mean quantities and first order statistics of our simulations where compared to those of [41] and the agreement is quite good. The profile of the mean velocity in wall units is shown in Fig. 2. The profile for the Reynolds stress $-\overline{u'v'}$ shows that the maximum (in absolute value) is located at approximately $y^+ = 30$, in the outer limit of the buffer layer (sse Fig. 3).

3.2. Results

The LCS were extracted from the turbulent velocity field data described in the previous section. A calculation of FSLE field in the entire turbulent channel was conducted in order to understand the statistical properties of the FSLE field in this class of turbulent
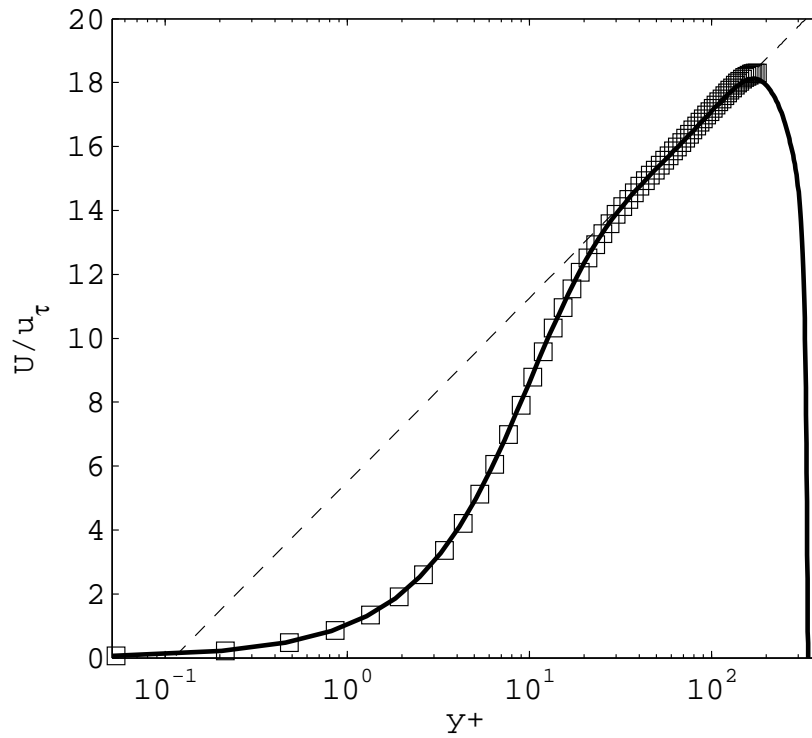
Figure 2. Mean velocity profile $U(y)/u_\tau$. Solid line: our simulations; squares: [41]; dashed line: logarithmic profile $U(y)/u_\tau = 2.5 \log(y^+) + 5.5$.
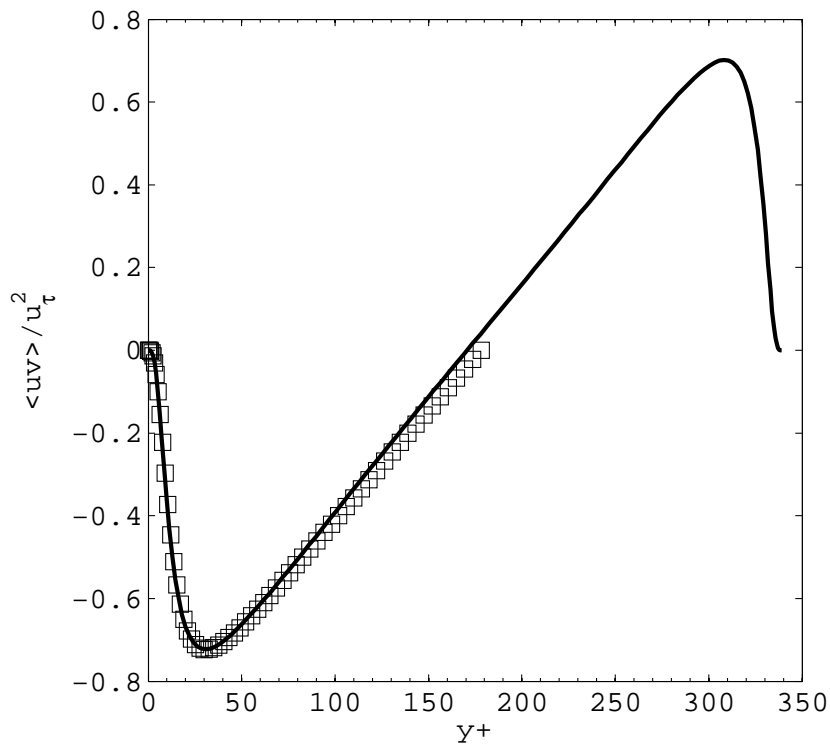

Figure 3. Reynolds stress $\overline{u'v'}$ profile at $Re_\tau = 180$. Solid line: our simulations; squares: [41] (given up to the channel centerline).

Table 1. Simulation parameters. Quantities with $^+$ refer to wall units. L_x, 2δ and L_z are the domain sizes in the x, y and z directions. Δx^+, Δy^+ and Δz^+ are the respective spatial resolutions (given at the first point above the wall for the y case), and n_x, n_y and n_z the corresponding number of grid points. $Re = U\delta/\nu$ is the Reynolds number based on the channel center mean speed, whereas $Re_\tau = u_\tau\delta/\nu$ is the viscous Reynolds number. The nominal value is an input to the computer code, and the actual value comes by using Eq. (7) for the computed mean profile $U(y)$.

Re channel center	4000	Re_τ nominal	180	Re_τ actual	172
L_x	4π	δ	1	L_z	$\frac{4}{3}\pi$
L_x^+	2166.61	δ^+	0.0058	L_z^+	722.20
n_x	128	n_y	129	n_z	128
Δx^+	17.06	Δy^+	0.005	Δz^+	5.6867

Table 2. FSLE calculation parameters. dt is the integration time step and Δt the maximum integration time.

Calculation	d_0	d_f/d_0	Δt	dt
Complete channel	0.024	20	172	0.05
LCS subdomain	0.003	67	10	0.05

flows. A subsequent calculation in a subdomain of the channel was used to extract the LCS in that subdomain for a sequence of time instants. The setup of both calculations is shown in table 2.

3.2.1. The 3d FSLE field. The 3d backward FSLE field for the entire channel was calculated at a single time instant in the statistically steady state. The initial and final distances d_0 and d_f were chosen as a balance between encompassing the widest possible range of scales of motion (measured by the ratio d_f/d_0), and adequate resolution and computational cost. The initial distance is of the order of $4\delta^+$ and the final distance of the order of 0.5δ so that the ratio of scales, d_f/d_0, is approximately $Re_\tau/8$.

Figure 4 shows an instantaneous configuration of the FSLE values in a streamwise/wall-normal plane. Maxima of the FSLE field appear to be organized into sloping structures located in the region $20 < y^+ < 100$. This organization bears resemblance to the widely accepted picture of organized structures in wall turbulence where the outer region is dominated by packets of sloping hairpin vortices [40, 38]. The channel center is devoid of high FSLE values but coherent patches of low FSLE values can still be observed.

A cross-stream FSLE profile is obtained by averaging the 3d field over the periodic directions x and z. It is shown in Fig. 5. The profile is symmetric about the channel centerline and shows a maximum at approximately $y^+ = 30$, at the same location of the maximum in the Reynolds stress $-\overline{u'v'}$. Because of the periodic boundary conditions in the x and z directions the average profiles along these directions are
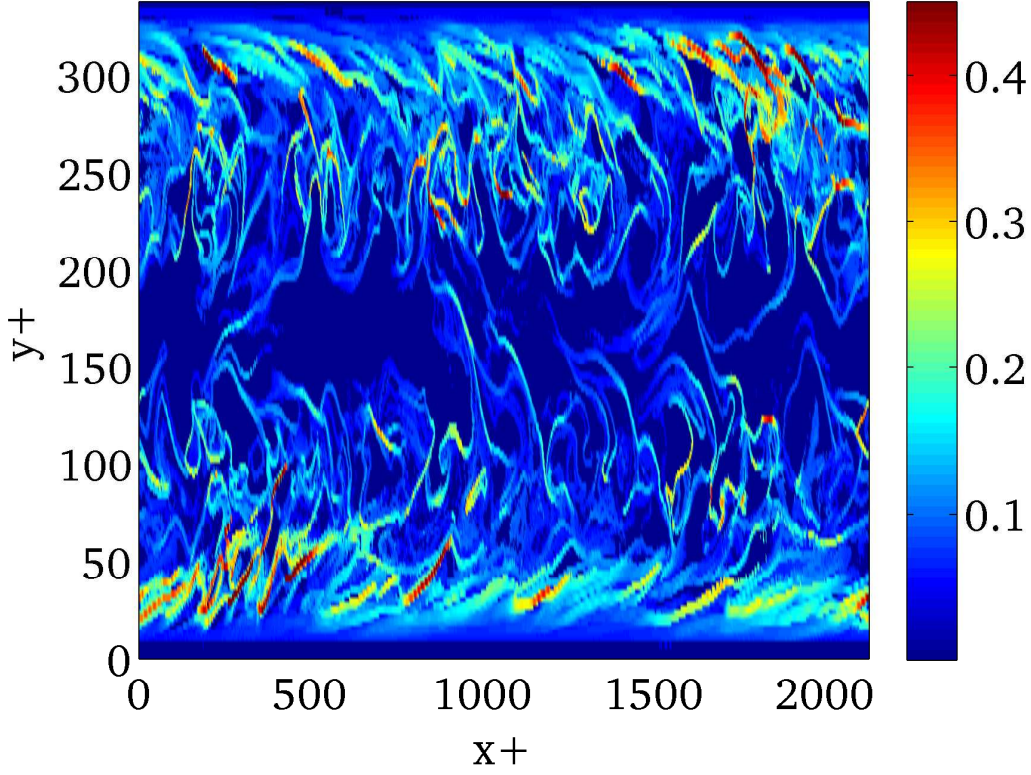
Figure 4. FSLE values shown on a streamwise/wall-normal plane in the turbulent channel. Walls are at the top and bottom of the figure. Mean velocity is towards the right.

rather unstructured, and we resort to two-point correlation functions to quantify the statistical structure properties. For each plane parallel to the walls, i.e. for each value of y^+, we compute the fluctuations of the FSLE values around the average in that plane: $\Lambda(x^+, y^+, z^+) \equiv \lambda(x^+, y^+, z^+) - \langle \lambda(x^+, y^+, z^+) \rangle_{x^+, z^+}$. From this quantity we define the streamwise $R_{xx}(y^+; \bar{x}^+)$ correlation function as:

$$R_{xx}(y^+; \bar{x}^+) = \frac{\langle \Lambda(x^+, y^+, z^+) \Lambda(x^+ + \bar{x}^+, y^+, z^+) \rangle_{x^+, z^+}}{\langle \Lambda(x^+, y^+, z^+)^2 \rangle_{x^+, z^+}} \tag{8}$$

and the spanwise $R_{zz}(y^+; \bar{z}^+)$ correlation function

$$R_{zz}(y^+; \bar{z}^+) = \frac{\langle \Lambda(x^+, y^+, z^+) \Lambda(x^+, y^+, z^+ + \bar{z}^+) \rangle_{x^+, z^+}}{\langle \Lambda(x^+, y^+, z^+)^2 \rangle_{x^+, z^+}} \ . \tag{9}$$

In the above equations the averages are over the periodic directions x^+ and z^+. The correlations are shown in Figs. 6 and 7 at different distances from the walls: one smaller, one larger, and one approximately coincident with the location of the maximum Reynolds stress. These functions reveal sizes and organization of the different structures in the Lagrangian FSLE field, to be contrasted with Eulerian correlation functions in the same system [42].
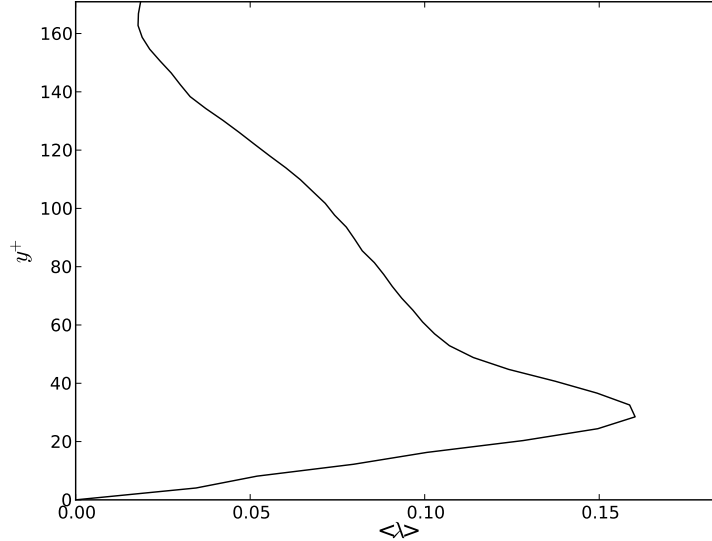
Figure 5. FSLE profile averaged over (x, z), as a function of the cross-stream normalized coordinate y^+. Only half of the channel is shown since the profile is quasi-symmetric about the channel centerline.

Close to the wall ($y^+ = 12.2$), viscous effects make the structures smooth and extended along the streamwise direction (see the long correlation length for this case in Fig. 6), forming streaks. In the transverse direction z^+ the oscillations seen in R_{zz} for $y^+ = 12.2$ indicate an approximately periodic arrangement of the streaks [22], with a spacing in the range $100 - 150$ wall units. This pattern of organization is similar to what is seen in Eulerian descriptions [42, 38]. At planes further away from the wall ($y^+ = 28.4$ and $y^+ = 122.1$ in Figs. 6 and 7), correlation functions in both directions become shorter ranged, and periodic features are progressively lost. This corresponds to a rather disordered distribution of structures, each with a typical size related to the width of the correlation functions, i.e. of the order of 50 wall units, as also seen in Fig. 4.

3.2.2. The 3d LCS. The previous description summarized the statistical properties of the different structures appearing in an instantaneous FSLE field. To make further progress we now extract three-dimensional attracting LCSs in a region of the channel at a series of time instants. The extraction domain had dimensions $L_x^+ \times L_y^+ \times L_z^+ = 103 \times 129 \times 124$. The initial separation d_0 and distance ratio d_f/d_0 were increased from the previous calculation to improve the resolution and extract smoother structures, but sacrificing a complete view of 3d LCS in the turbulent channel. The extraction threshold was set to $s = 50000$, a compromise value between speed and cost of extraction and continuity of the extracted surfaces. The FSLE fields were calculated for an interval of 1.5 time units with a time step of 0.1 units.
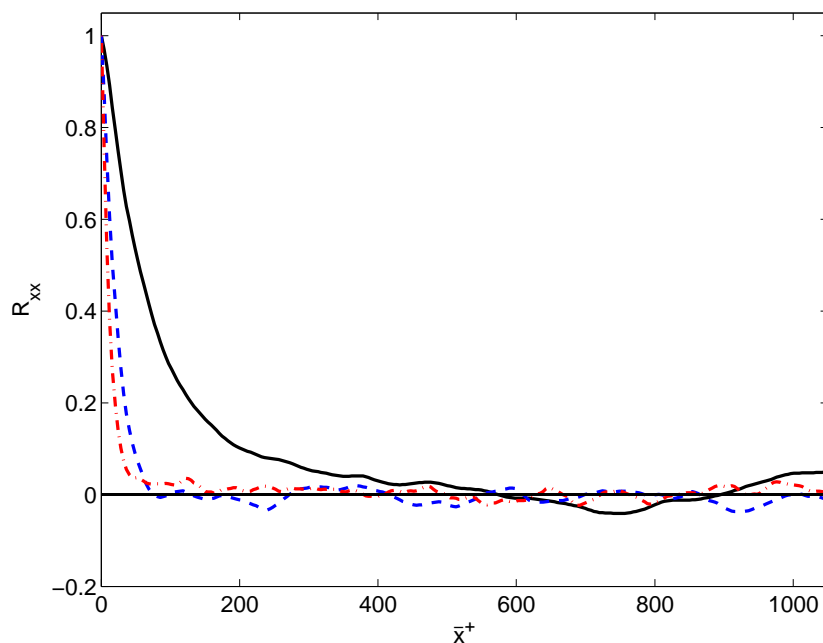
Figure 6. Streamwise correlation function $R_{xx}(y^+; \bar{x}^+)$ as a function of the streamwise separation $\bar{x}^+$, at three distances from the lower wall: Continuous black line: $y^+ = 12.2$; blue dashed line $y^+ = 28.4$; red dot-dashed line: $y^+ = 122.1$.
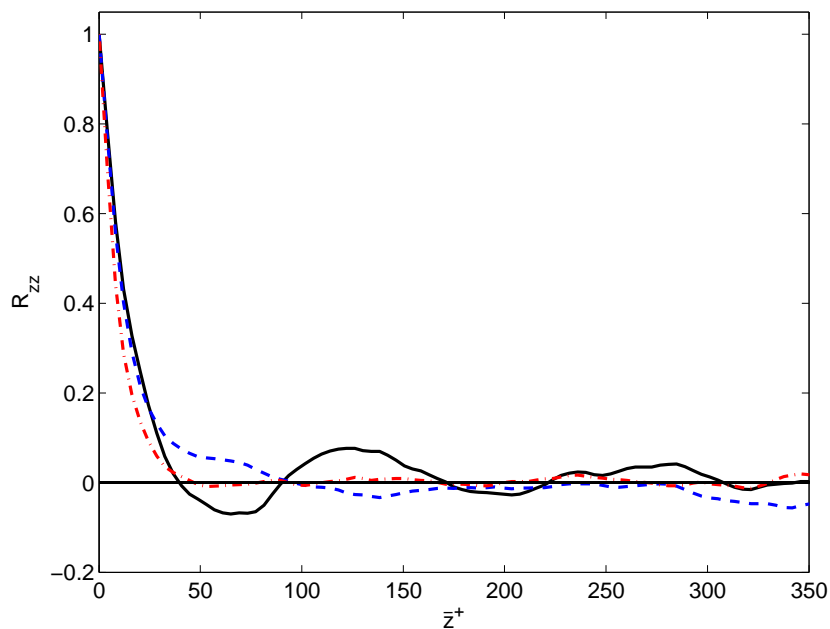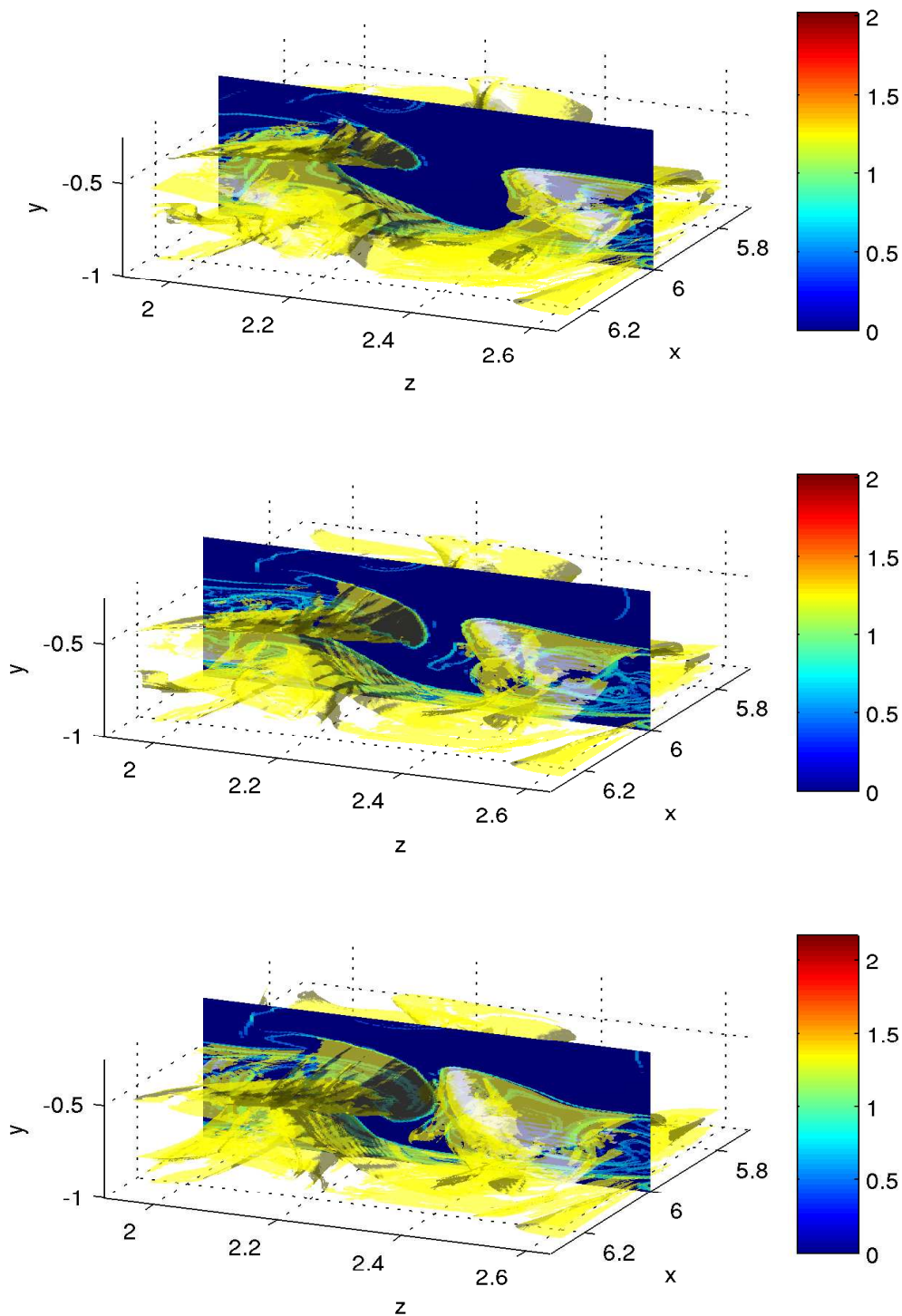

Figure 7. Spanwise correlation function $R_{zz}(y^+; \bar{z}^+)$ as a function of the spanwise separation $\bar{z}^+$, at three distances from the lower wall: Continuous black line: $y^+ = 12.2$; blue dashed line $y^+ = 28.4$; red dot-dashed line: $y^+ = 122.1$.

Figure 8. 3d attracting LCS in the channel flow together with a FSLE map at the fixed plane $x = 6.0$. Time goes from top to bottom, at intervals of 0.1 time units. The flow direction is in the positive x direction in each panel, and a wall is at the bottom. The sequence shows how one of the flow structures is advected and passes through the $x = 6.0$ plane.

3d LCSs are rendered in Fig. 8, in a sequence of time instants, as they pass through the calculation domain. They have a clearly 3d shape and move with the flow. The LCS seem to create a boundary between the inner turbulent region and the outer region that is practically devoid of FSLE. The highest LCS have δ-scale heights above the wall, and have a distinct mushroom shape enclosing the regions of the channel closer to the wall, where high FSLE values can be found. Near the wall, the LCS adopt the shape of sheets parallel to it, which reflects the high rates of shear that occur in that region. These sheets form the base of the mushroom-shaped excursions up to the channel center.

4. Oceanic flow

Contrarily to the turbulent flow of the previous section, large scale oceanic flows, naturally turbulent, can be considered as almost 2d due to rotation and stratification effects. This fact makes the theory of 2d turbulence a very important tool to understand the ocean processes that occur at large scales. The main characteristic of 2d turbulence is the existence of an inverse energy cascade, from the small to the large scales and a direct enstrophy cascade. This cascade manifests itself by the creation of large coherent vortices, and by the process of filamentation by which strain regions in the boundaries of the vortices produce lines of vorticity that are continuously stretched and deformed by the flow, concentrating the vorticity gradient in the small scales. This behavior is often observed in oceanic flows thereby confirming the importance of the 2d turbulent processes.

4.1. Data

The Benguela ocean region (Fig. 9) is situated off the west coast of southern Africa. It is characterized by a substantial mesoscale activity in the form of eddies and filaments, and also by the northward drift of Agulhas eddies.

The velocity data set comes from a regional ocean model (ROMS) simulation of the Benguela Region [43]. ROMS [44, 45] is a split-explicit, free-surface, topography following model. It solves the incompressible primitive equations using the Boussinesq and hydrostatic approximations. Potential temperature and salinity transport are included by coupling advection/diffusion schemes for these variables. The model was forced with climatological data. The data set area extends from 12°S to 35°S and from 4°E to 19°E (see Fig. 9). The velocity field $\mathbf{u} = (u, v, w)$ consists of two years of daily averaged zonal (u), meridional (v), and vertical velocity (w) components, stored in a three-dimensional grid with an horizontal resolution of 1/12 degrees ($\sim$ 8 km), and 32 vertical terrain-following levels. Additional details can be found in [31].
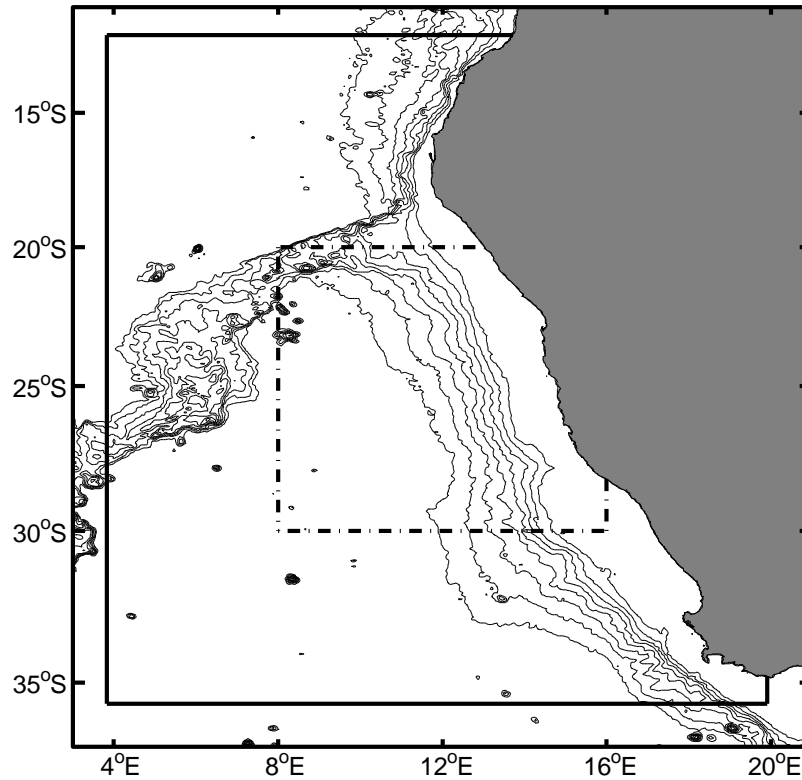
Figure 9. Benguela ocean region. Grey region is Southwestern Africa. The velocity field domain is limited by the continuous black line. The FSLE calculation area is limited by the dash-dot black line. Bathymetric contour lines are from ETOPO1 global relief model [46] from 0 m depth up to 4000 m at intervals of 500 m.

4.2. Results

4.3. Three-dimensional FSLE field

The three-dimensional FSLE fields were calculated for a 30 day period starting September 17 of year 9, with snapshots taken every 2 days. The fields were calculated for an area of the Benguela ocean region between latitudes 20°S and 30°S and longitudes 8°E to 16°E (see Fig. 9). The calculation domain extended vertically from 20 up to 580 m of depth. Both backward and forward calculations were made in order to extract the attracting and repelling LCS.

Figure 10 displays the vertical profile of the average FSLE for the 30 day period. The small differences between the backward and the forward values are due to the different intervals of time involved in their calculation. There is a general decrease with depth, with a notable peak in the profiles at about 100 m. The reason for this local maximum in the FSLE profiles is not clear but it could be due to increased vertical shear enhancing the mixing rates at those depths [31].

In the left panel of Fig. 11 a snapshot of the attracting LCSs for day 1 of the calculation period is shown. The structures appear as thin vertical curtains, most of them extending throughout the whole depth of the calculation domain. The horizontal
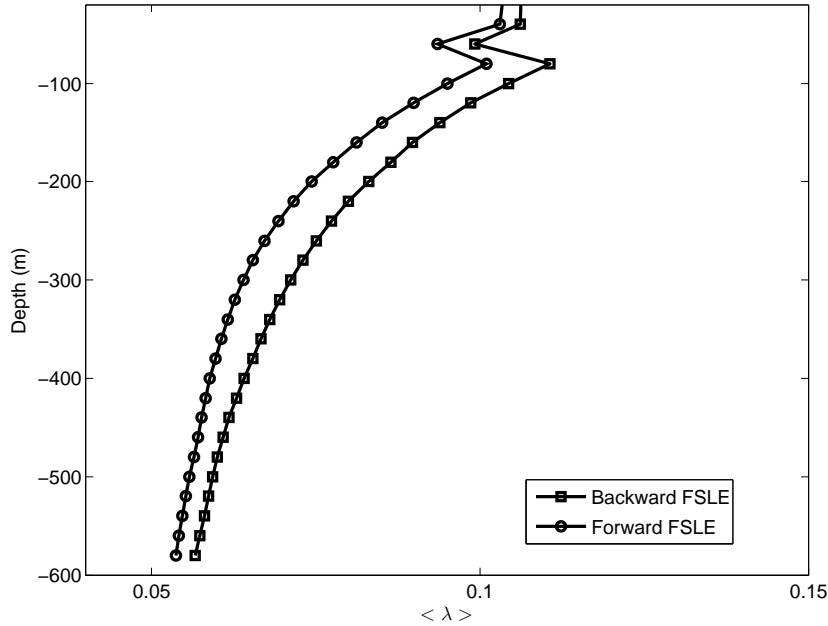
Figure 10. Vertical profile of a 30 day average of backward (squares) and forward (circles) FSLE. The 30 day average 3d field was further spatially averaged over each horizontal layer to produce the vertical profiles.

slices of the FSLE field in Fig. 11 (left panel) show that the attracting LCS fall on the maximum FSLE field lines. The atracting and repelling LCS (Fig. 11, right panel) populate the calculation region, testifying the enhanced mixing activity that is known to occur in that particular ocean region. The quite entangled "web" in which attracting and repelling LCSs intersect mutually provides the skeleton for the barriers and pathways controlling transport [6, 11].

At this point, it may help to stress the differences between the Eulerian and Lagrangian detection of coherent structures. This can be seen in Fig. 12 where the boundaries of a mesoscale eddy are shown using the Q-criterion and the attracting and repelling LCS. The Q-criterion [47] uses the second invariant of $\nabla \mathbf{u}$:

$$Q = \frac{1}{2}(\|\mathbf{\Omega}\|^2 - \|\mathbf{S}\|^2), \tag{10}$$

where $\|\mathbf{\Omega}\|^2 = \mathrm{tr}(\mathbf{\Omega}\mathbf{\Omega}^{\mathrm{T}})$, $\|\mathbf{S}\|^2 = \mathrm{tr}(\mathbf{S}\mathbf{S}^{\mathrm{T}})$, and $\mathbf{\Omega}$, $\mathbf{S}$ are the antisymmetric and symmetric components of $\nabla \mathbf{u}$, to identify regions where rotation dominates strain ($Q > 0$), commonly identified with coherent vortices, and strain dominated regions ($Q < 0$). We refer the reader to [48] and [49] for reviews and criticism of several Eulerian criteria.

Eulerian and Lagrangian measures limit approximately the same region, but are substantially different. The Q-criterion is related to the instantaneous configuration of the second invariant of $\nabla \mathbf{u}$ and therefore conveys only local information about fluid flow processes. The Lagrangian perspective, on the other hand, provides an integration of the temporal evolution of material properties of the flow, e.g. material transport, and
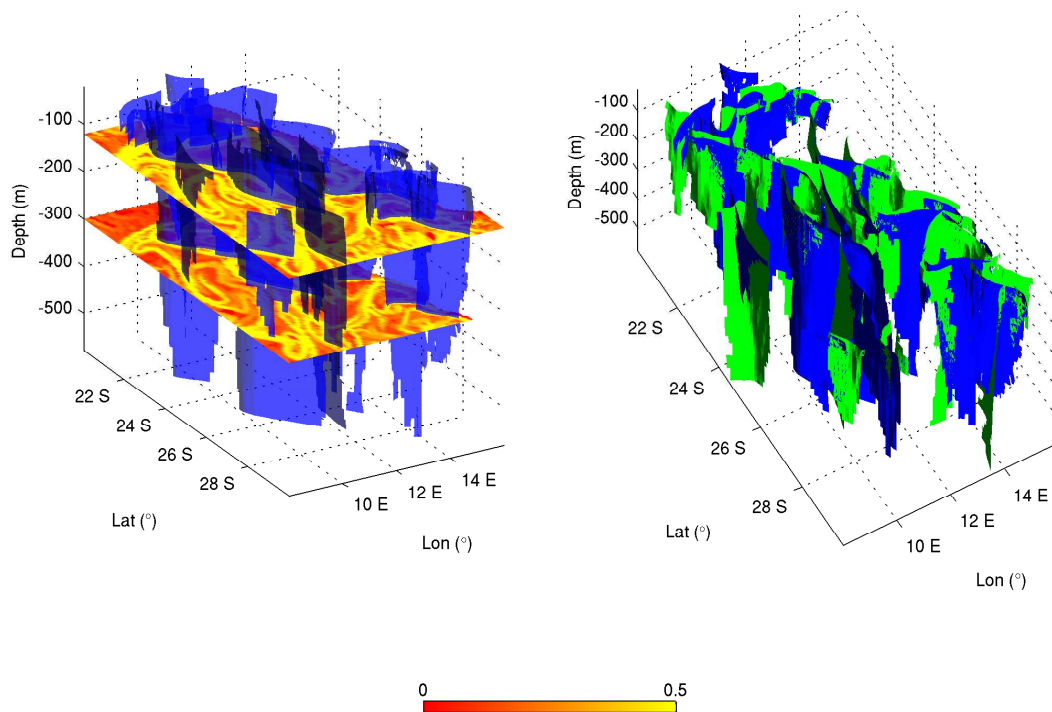
Figure 11. 3d LCS in the Benguela region for day 1 of the calculation period. Left panel: Attracting LCS together with horizontal slices of the backward FSLE field at 120 m and 300 m depth. Right panel: Attracting (blue) and repelling (green) LCS. Colorbar refers to colormap of horizontal slices in the left panel. The units of the colorbar are day^{-1}.

thus should give more meaningful information about the processes that rely on ocean material transport.

This issue can be further explored by looking at a filamentation event (described more extensively in [31]). A set of particles were released inside the eddy at day 1 at a depth of 50 m. At day 11 of the calculation period (see Fig. 13), they have formed a filament that is expelled from the eddy, so that particles clearly cross the Q-criterion isosurface. This shows that the Eulerian criteria is inadequate as an indicator of regions of material transport in the flow. On the contrary, it can be observed that the Lagrangian description of the eddy boundaries does bear relation with material transport into and out of the eddy, since the particle filament leaves the enclosed region that we associate with the mesoscale eddy by following one of the identified Lagrangian boundaries.

5. Conclusions

Lyapunov exponents are useful to identify Lagrangian Coherent Structures in turbulent flows. These constitute the pattern determining the pathways of particle transport in
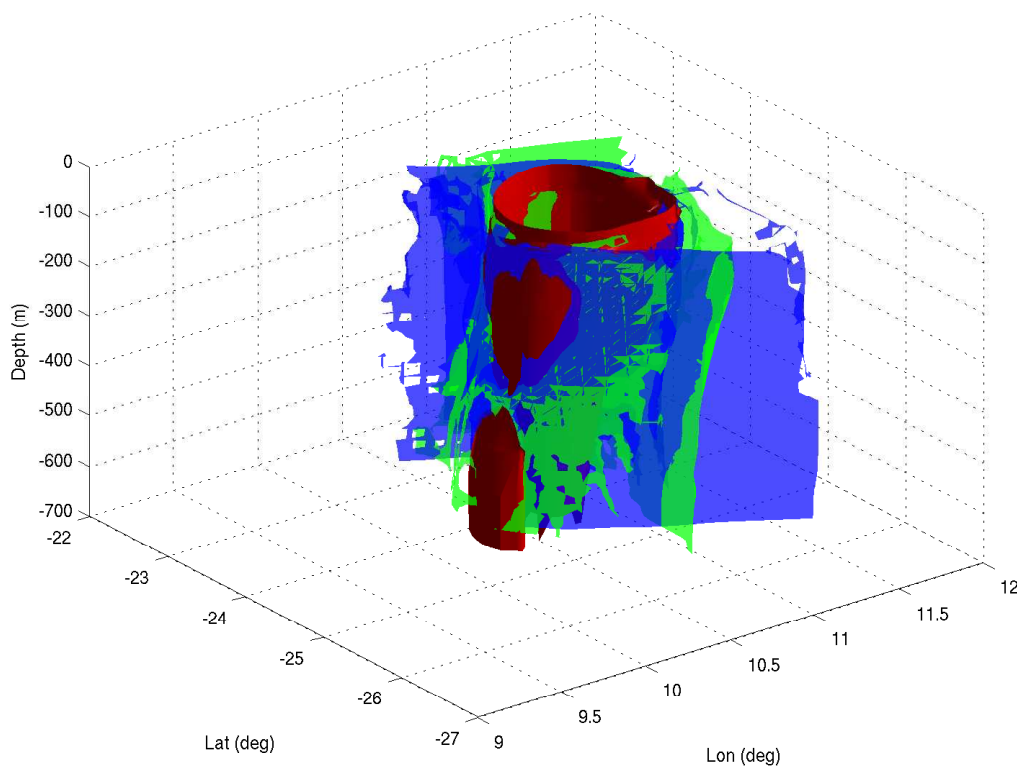
Figure 12. Attracing (blue) and repelling (green) LCS on day 1 of the calculation period together with Q-criterion isosurface at $Q = 10^{-10}$ (red).

the flow. They strongly influence the transport and mixing properties in the fluid.

In this paper we have used a particular type of Lyapunov exponents, the so-called Finite-Size Lyapunov exponents, to identify LCS in 3d flows. The finite size Lyapunov exponent was used to measure the rate of streching of initially nearby fluid particles in the flow domain and the Lagrangian coherent structures where identified as the the ridges of the FSLE field. These ridges were filtered in order to retain only the strongest attracting or repelling structures.

In a turbulent channel flow, the LCSs appear as mushroom-shaped excursions of near-wall sheet-like structures of a scale comparable to the channel width. They separate the channel into an interior region, where the FSLE attains high values, and an exterior region, showing low FSLE values. The distribution of LCS in the turbulent channel resembles the commonly accepted picture where upward excursions of near wall fluid coexist with inward rushes of mid-channel irrotational flow. Further work is necessary to elucidate the relations between LCS and fluid transport in these type of flows, not least because the visualization of 3d structures and transport in turbulence is a complex and time-consuming subject.

In a quasi-2d mesoscale oceanic flow, the LCSs appear as quasi-vertical surfaces highlighting the fact that dispersion in this case is mainly horizontal. The high mixing activity can be deduced from the proliferation of LCS in the flow domain and their
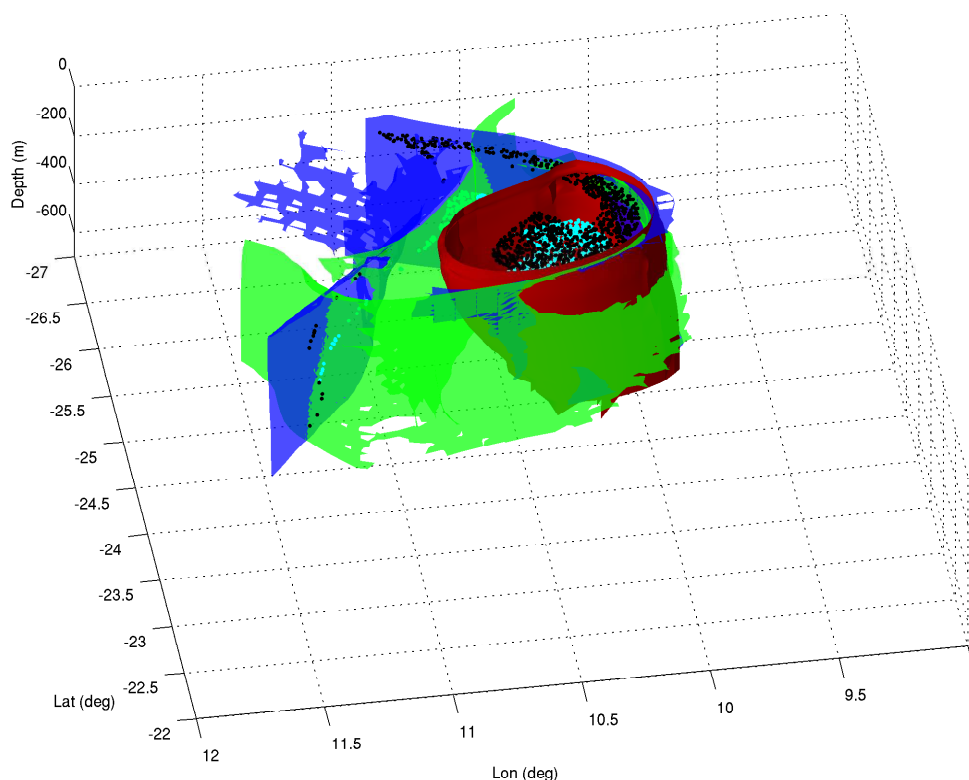
Figure 13. Attracing (blue) and repelling (green) LCS on day 11 of the calculation period together with Q-criterion isosurface at $Q = 10^{-10}$ (red). The particles (black dots) were released inside the eddy at day 1 at a depth of 50 m and are leaving now the eddy as a filament along the upper part of the attracting LCS.

mutual intersection. These LCS were seen to provide barriers and pathways to transport in the case of a mesoscale eddy, contrary to Eulerian measures that failed to provide indicative locations or directions of major transport events.

The results shown in this paper highlight the usefulness of Lyapunov analysis and dynamical systems theory as a tool to study transport and mixing in fluid flows, through the concept of Lagrangian coherent structures.

Acknowledgements

References

[1] Artale V, Boffetta G, Celani A, Cencini M and Vulpiani A 1997 *Phys. Fluids* **9** 3162–3171

[2] Aurell E, Boffetta G, Crisanti A, Paladin G and Vulpiani A 1997 *J. Phys. A* **30** 1–26

[3] Boffetta G, Lacorata G, Redaelli G and Vulpiani A 2001 *Physica D* **159** 58–70

[4] Lapeyre G 2002 *Chaos* **12(3)** 688–698

[5] Boffetta G, Celani A, Cencini A, Lacorata G and Vulpiani A 2000 *Chaos* **10** 50–60

[6] d'Ovidio F, Fernández V, Hernández-García E and López C 2004 *Geophys. Res. Lett.* **31** L17203

[7] Poje A C, Haza A C, Özgökmen T M, Magaldi M G and Garraffo Z D 2010 *Ocean Modell.* **31** 36–50

[8] Haller G 2000 *Chaos* **10(1)** 99–108

[9] Haller G and Yuan G 2000 *Physica D* **147** 352–370

[10] Joseph B and Legras B 2002 *J. Atm. Sci.* **59** 1198–1212

[11] Mancho A M, Small D and Wiggins S 2006 *Phys. Rep.* **437** 55–124

[12] d'Ovidio F, Isern J, López C, Hernández-García E and García-Ladona E 2009 *Deep-Sea Res. I* **56** 15–31

[13] Peacock T and Dabiri J 2010 *Chaos* **20** 017501 (pages 3)

[14] Shadden S C, Lekien F and Marsden J E 2005 *Physica D.* **212** 271–304

[15] Lekien F, Shadden S C and Marsden J E 2007 *J. Math. Phys.* **48** 065404

[16] Haller G 2011 *Physica D* **240** 574–598

[17] Molcard A, Poje A and Özgökmen T 2006 *Ocean Modell.* **12** 268–289

[18] Branicki M and Wiggins S 2010 *Nonlinear Processes Geophys* **17** 1–36

[19] du Toit P and Marsden J 2010 *J. Fixed Point Theory Appl.* **7**(2) 351–384

[20] Tang W, Chan P W and Haller G 2011 *Journal of Applied Meteorology and Climatology* **50** 325–338

[21] Tallapragada P, Ross S D and Schmale III D G 2011 *Chaos* **21** 033122 ISSN 10541500

[22] Green M A, Rowley C W and Haller G 2007 *J. Fluid Mech.* **572** 111–120

[23] Haller G 2001 *Physica D* **149** 248–277

[24] Bakun A 1996 *Patterns in the ocean. Ocean processes and marine population dynamics* (California Sea Grant College System, NOAA and Centro de Investigaciones Biolgicas del Noroeste, La Paz, BCS Mxico)

[25] Rossi V, López C, Sudre J, Hernández-García E and Garçon V 2008 *Geophys. Res. Lett.* **35** L11602

[26] Rossi V, López C, Hernández-García E, Sudre J, Garçon V and Morel Y 2009 *Nonlinear Processes Geophys* **16** 557–568

[27] Tew Kai E, Rossi V, Sudre J, Weimerskirch H, López C, Hernández-García E, Marsac F and Garçon V 2009 *Proc. Natl. Acad. Sci. U.S.A.* **106** 8245–8250

[28] Branicki M and Malek-Madani R 2010 *Nonlinear Processes in Geophysics* **17** 149–168

[29] Branicki M, Mancho A M and Wiggins S 2011 *Physica D* **240** 282 – 304

[30] Özgökmen T M, Poje A C, Fischer P F and Haza A C 2011 *Ocean Modell.* **39** 311–331

[31] Bettencourt J, López C and Hernández-García E 2012 *Ocean Modell.* **51** 73–83

[32] Beron-Vera F, Olascoaga M J, Brown M G, Koçak H and Rypina I I 2010 *Chaos* **20** 017514

[33] Pouransari Z, Speetjens M and Clercx H 2010 *J. Fluid Mech.* **654** 5–34

[34] Schultz T, Theisel H and Seidel H P 2010 *IEEE Transactions on Visualization and Computer Graphics* **16** 109–119

[35] Eberly D, Gardner R, Morse B, Pizer S and Scharlach C 1994 *Journal of Mathematical Imaging and Vision* **4** 353–373

[36] Sadlo F and Peikert R 2007 *IEEE Transactions on Visualization and Computer Graphics* **13** 1456–1463

[37] Tennekes H and Lumley J L 1972 *A First Course in Turbulence* (The MIT Press)

[38] Robinson S K 1991 *Annu. Rev. Fluid Mech.* **23** 601–639

[39] Holmes J, Lumley J L and Berkooz G 1998 *Turbulence, Coherent Structures, Dynamical Systems and Symmetry* Cambridge Monographs on Mechanics (Cambridge University Press)

[40] Adrian R J 2007 *Phys. Fluids* **19** 041301

[41] Moser R D, Kim J and Mansour N N 1999 *Phys. Fluids* **11** 943–945

[42] Kim J, Moin P and Moser R 1987 *Journal of Fluid Mechanics* **177** 133–166

[43] Le Vu B, Gutknecht E, Machu E, Dadou I, Veitch J, Sudre J, Paulmier A and Garçon V 2011 *submitted to JMR*

[44] Shchepetkin A F and McWilliams J C 2003 *J. Geophys. Res.* **108** 3090

[45] Shchepetkin A F and McWilliams J C 2005 *Ocean Modell.* **9** 347–404

[46] Amante C and Eakins B W 2009 ETOPO1 1 arc-minute global relief model: Procedures, data sources and analysis NOAA Technical Memorandum NESDIS NGDC-24

[47] Hunt J C R, Wray A A and Moin P 1988 Eddies, streams and convergence zones in turbulent flows Tech. Rep. CTR-S88 Center for Turbulence Research, Standford University 193–208

[48] Jeong J and Hussain F 1995 *J. Fluid Mech.* **285** 69–94

[49] Haller G 2005 *J. Fluid Mech.* **525** 1–26